Available online at www.sciencedirect.com
SCIENCE DIRECT®
Journal of Sound and Vibration 289 (2006) 999–1018
JOURNAL OF SOUND AND VIBRATION
www.elsevier.com/locate/jsvi

Analysis and optimization of aerodynamic noise in a centrifugal compressor

Hyosung Sun*, Hyungki Shin, Soogab Lee

*Center for Environmental Noise and Vibration Research, School of Mechanical and Aerospace Engineering,
Seoul National University, San 56-1, Shinlim-dong, Kwanak-gu, Seoul 151-742, Korea*

Received 18 March 2004; received in revised form 18 November 2004; accepted 7 March 2005

Abstract

The numerical methods for the performance analysis and the noise prediction of the centrifugal compressor impeller are developed, which are coupled with the optimization design methodology consisting of response surface method, statistical approach, and genetic algorithm. Navier–Stokes equations with the two-equation (k–ω) turbulence model are applied to calculate impeller aerodynamic characteristics, and Ffowcs Williams–Hawkings formulation and boundary element method are used to predict the impeller aerodynamic noise on the basis of impeller flow field results. The computational codes are verified through the comparison of measured data. The quadratic response surface model with D-optimal three-level factorial experimental design points is constructed to optimize the impeller geometry for the advanced centrifugal compressor, and it is shown that the quadratic model exhibits a reasonable fitting quality resulting in the impeller blade design with the high performance and the low far-field noise level. The influences of selected design variables and their mutual interactions as well as the effects of various objective functions and constraints on the impeller performance and the impeller noise are also examined as a result of the optimization process.

---

*Corresponding author. Tel.: +82 2 880 7384; fax: +82 2 875 4360.
E-mail address: aerosun@snu.ac.kr (H. Sun).

0022-460X/$ - see front matter © 2005 Elsevier Ltd. All rights reserved.
doi:10.1016/j.jsv.2005.03.004

1. Introduction

The acoustic consideration of the centrifugal compressor has become imperative due to regulations and the ubiquitous call for environment-friendly products. The centrifugal compressor impeller designers have relied heavily on their experience or prediction codes that supply only a rough estimation to consider the noise performance as a parameter from the design process. Owing to the advances in computational fluid dynamics (CFD) and noise prediction tools, however, the aerodynamic/acoustic shape design optimization of the impeller blade has been initiated. The automation of the aerodynamic/acoustic shape design by coupling numerical methods with the design framework enables the overall design cost to be reduced. Since various shapes can be tested in a numerical environment, the design result can be improved drastically compared with that obtained by man-in-loop activities. From this point of view, the present research is focused on suggesting a comprehensive optimization tool that incorporates the latest developments in fluid dynamics, aeroacoustics, and optimization technique.

Response surface method (hereafter, RSM) is a collection of statistical and mathematical techniques useful for developing and improving the optimization process [1,2]. RSM has drawn much attention because of its efficiency and advantages: (1) It smoothes out the high-frequency noise of the objective function and is expected to find a solution near the global optimum. (2) Various objectives and constraints can be attempted in the design process without additional numerical computations. (3) It can be effectively applied to multi-disciplinary design optimization (MDO) problems with many objectives and constraints. (4) It does not require a modification in analysis codes. However, there are some drawbacks to RSM. The range of design parameters highly affects the fitting capabilities of the response model. The wide range may increase prediction errors such that the predicted performance cannot be exactly obtained. RSM has a limitation on the number of design variables, because the computation time for constructing the response model is proportional to the square of the number of design parameters.

Navier–Stokes solver is employed to compute the impeller performance, and the frequency domain approach of Ffowcs Williams–Hawkings (hereafter, FW–H) formulation applicable to the impeller blade design is chosen as the governing equation for the noise prediction. The optimization procedure is explained in detail with the additional discussion about the experimental point selection method. Since the optimization method involves statistics, some discussions of regression coefficients appearing in statistical analysis are given. The developed numerical method is applied to the centrifugal compressor impeller shape design and the design variables having a dominant effect on the performance and the noise are also analyzed.

2. Flow solver

The governing equations are 3D, unsteady, compressible Navier–Stokes equations and can be written in conservation law form as

$$\frac{\partial \rho}{\partial t} + \frac{\partial}{\partial x_j}(\rho u_j) = 0,$$

$$\frac{\partial}{\partial t}(\rho u_i) + \frac{\partial}{\partial x_j}(\rho u_i u_j) = -\frac{\partial p}{\partial x_i} + \frac{\partial \hat{\tau}_{ij}}{\partial x_j},$$

$$\frac{\partial \rho e}{\partial t} + \frac{\partial}{\partial x_j}(\rho e u_j) = -\frac{\partial p u_j}{\partial x_j} + \frac{\partial}{\partial x_j}[u_i \hat{\tau}_{ij} - q_j], \tag{1}$$

where ρ is the density, t is the time, $x_j(= x, y, z)$ are the Cartesian coordinates, $u_j(= u, v, w)$ are the Cartesian components of the velocity, p is the static pressure, e is the total energy, and $\hat{\tau}_{ij}$ is composed of the molecular and Reynolds stresses defined as

$$\hat{\tau}_{ij} = 2\mu(S_{ij} - S_{kk}\delta_{ij}/3) + \tau_{ij},$$

$$\tau_{ij} = 2\mu_T(S_{ij} - S_{kk}\delta_{ij}/3) - 2\rho k \delta_{ij}/3,$$

$$S_{ij} = \frac{1}{2}\left(\frac{\partial u_i}{\partial x_j} + \frac{\partial u_j}{\partial x_i}\right), \tag{2}$$

where μ is the laminar viscosity, μ_T is the turbulent eddy viscosity, δ_{ij} is the Kronecker delta, S_{ij} is the mean strain-rate tensor, and q_j is the total heat-flux rate defined as

$$q_j = -\left(\frac{\gamma}{\gamma - 1}\right)\left(\frac{\mu}{Pr} + \frac{\mu_T}{Pr_T}\right)\frac{\partial T}{\partial x_j}, \tag{3}$$

where γ is the ratio of the specific heats, Pr is the laminar Prandtl number, Pr_T is the turbulent Prandtl number, and T is the static temperature. The perfect gas equation of state is introduced to complete the set of compressible equations as

$$p = \rho(\gamma - 1)\left[e - \frac{1}{2}u_i u_i\right]. \tag{4}$$

In this work, the original k–ω turbulence model is evaluated to predict the viscous turbulent flow of the centrifugal compressor impeller. It has the transport equations off the turbulent kinetic energy, k and the specific dissipation rate, ω as

$$\frac{\partial \rho k}{\partial t} + \frac{\partial}{\partial x_j}(\rho k u_j) = \tau_{ij}\frac{\partial u_i}{\partial x_j} - \beta^* \rho \omega k + \frac{\partial}{\partial x_j}\left[(\mu + \sigma_{k_1}\mu_T)\frac{\partial k}{\partial x_j}\right],$$

$$\frac{\partial \rho \omega}{\partial t} + \frac{\partial}{\partial x_j}(\rho \omega u_j) = \frac{\gamma_1}{v_T}\tau_{ij}\frac{\partial u_i}{\partial x_j} - \beta_1 \rho \omega^2 + \frac{\partial}{\partial x_j}\left[(\mu + \sigma_{\omega_1}\mu_T)\frac{\partial \omega}{\partial x_j}\right], \tag{5}$$

where v_T is the turbulent kinematic viscosity and $\sigma_{k_1} = 0.5$, $\sigma_{\omega_1} = 0.5$, $\beta_1 = 0.075$, $\beta^* = 0.09$, and $\gamma_1 = \beta_1/\beta^* - \sigma_{\omega_1}\kappa^2/\sqrt{\beta^*}$, $\kappa = 0.41$ [3].

The governing equations are transformed in generalized coordinates and are solved with a finite volume method. With a backward Euler implicit method, the governing equations are discretized in time and linearized in delta form as

$$\left(\frac{I}{J\Delta t} + \left[\frac{\partial R}{\partial Q}\right]^n\right)\Delta Q = -R^n, \tag{6}$$

where I is the identity matrix, Δt is the time interval, n is the time step, J is the Jacobian of transformation, R is the residual of steady-state flow equations, Q is the vector of conservative variables $(\rho, \rho u, \rho v, \rho w, \rho e)^{\mathrm{T}}$, and $\Delta Q = Q^{n+1} - Q^{n}$.

For the calculation of the residual, convective terms are upwind-differenced based on Roe's flux difference splitting scheme [4] and viscous terms are central-differenced. MUSCL approach using a third-order interpolation is used to obtain a higher order of spatial accuracy [5]. For a temporal integration, AF-ADI scheme is adopted to solve Eq. (6) efficiently [6]. In order to analyze the flow unsteadiness due to the circumferential inlet and outlet pressure distortions of the centrifugal compressor impeller, the impeller grid is rotating at a constant angular velocity and the patched grids of the inlet duct and the vaneless diffuser are used to connect the impeller moving grid. The wall boundary conditions are applied explicitly with no-slip condition. The pressure is extrapolated from interior points and the other variables are specified from freestream values at the inflow, whereas the pressure is specified and the other variables are extrapolated from interior points at the outflow. The conservative interpolation method is used to apply the boundary conditions for patching across the impeller moving grid and fixed grids (inlet duct and vaneless diffuser) [7].

The data published by Eckardt [8] are chosen to validate the present numerical method. Eckardt performed the measurements for performance, pressure distribution along the shroud, and velocity field within the impeller. The measured data have been widely used to verify the computational code and also quoted in describing the flow characteristics along the impeller. The test impeller is a typical high-speed radial impeller (Eckardt 0-type impeller) and the geometry data are obtained from Schuster and Schmidt-eisenlohr [9]. The compressor of 20 impeller blades is operated at a rotational speed of 14,000 rev/min and the design mass flow rate is 5.32 kg/s. Fig. 1(a) displays Eckardt 0-type impeller for the radial discharge type. Its meridional blade contour and overall dimensions are given in Fig. 1(b), which also indicates five optical measuring planes, I–V for analyzing the impeller flow field [8]. In Fig. 1(b), R is the radius and S_m is the meridional position. Fig. 2 presents relative velocity distributions at measurement planes on hub-to-shroud surfaces at the half-pitch position for the design flow rate, and the comparisons between calculation results and measured data show a good agreement. In Fig. 2, w/u_2 is the ratio of the relative velocity, w to the rotational velocity of the impeller tip, u_2, b is the width of the measurement plane, and z is the vertical location of the measurement plane.

3. Acoustic prediction

It is widely known that the dipole due to the unsteady pressure fluctuation is the dominant source of the centrifugal compressor noise. The most prominent source of the dipole in the centrifugal compressor is the rotating impeller. FW–H equation of the point dipole assumption is used to define the noise source of the centrifugal compressor impeller [10].

$$p(\vec{x}, t) = \frac{\cos\theta f}{4\pi}\left\{\frac{\mathrm{i}\omega}{rc} + \frac{1}{r^2}\right\}\mathrm{e}^{\mathrm{i}\omega(t-r/c)}, \tag{7}$$

where $p(\vec{x}, t)$ is the acoustic pressure, $\vec{x}$ is the observer position vector, t is the observer time, $\cos\theta$ is the directivity factor, f is the source strength, ω is the radiated frequency, r is the distance

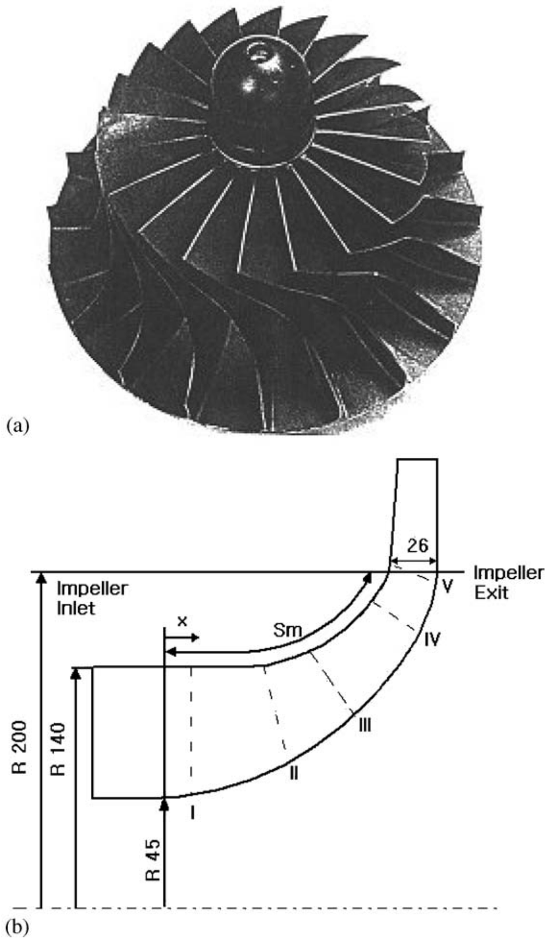

Fig. 1. (a) Configuration of Eckardt 0-type impeller (Ref. [16]) and (b) Measurement planes (Ref. [8]).

between the source and the observer point, and c is the speed of sound. The near- and far-field components are seen explicitly as $1/r^2$ and $1/r$ terms, respectively. The acoustic pressure boundary conditions which are the input data of boundary element analysis are obtained from the combination of FW–H formulation and the computed pressure spectrum of the impeller inlet and outlet (Fig. 3). The distributed pressure in the impeller inlet and outlet is divided by small grid elements and the pressure in the impeller inlet and outlet is represented by a point dipole which acts on that element. In order to define the aeroacoustic source of BEM, the source meshes are introduced in the impeller inlet and outlet. The acoustic values of these source meshes can be calculated by FW–H formulation (Eq. (7)), which are regarded as the noise source in BEM [11].

The indirect BEM in the frequency domain is used to predict the inner and outer noise propagations of the centrifugal compressor impeller. The boundary element method is based on expressing the acoustic pressure, $p(\vec{r})$ at a point within the acoustic medium as an integral over the boundary defining the acoustic domain, which is known as Helmholtz/Kirchhoff integral equation [12].

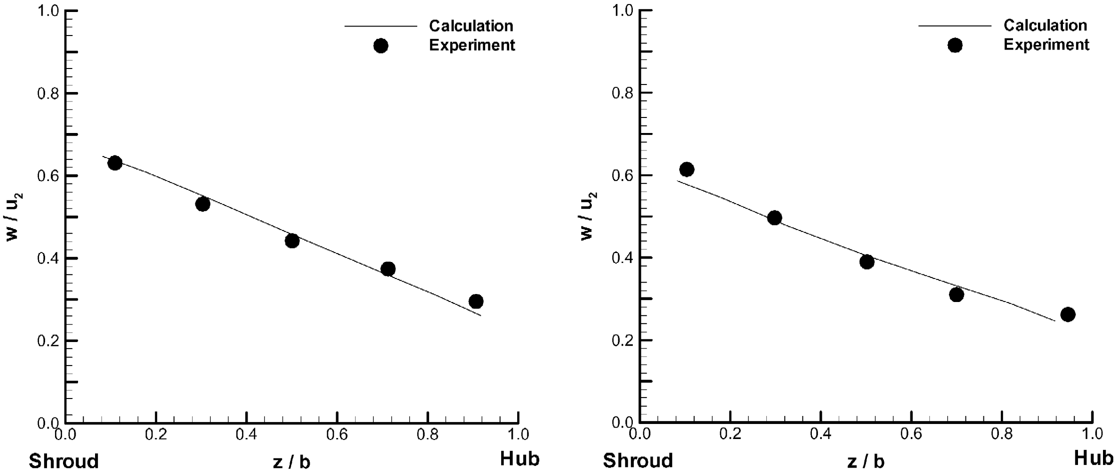

(a) Plane I (b) Plane II

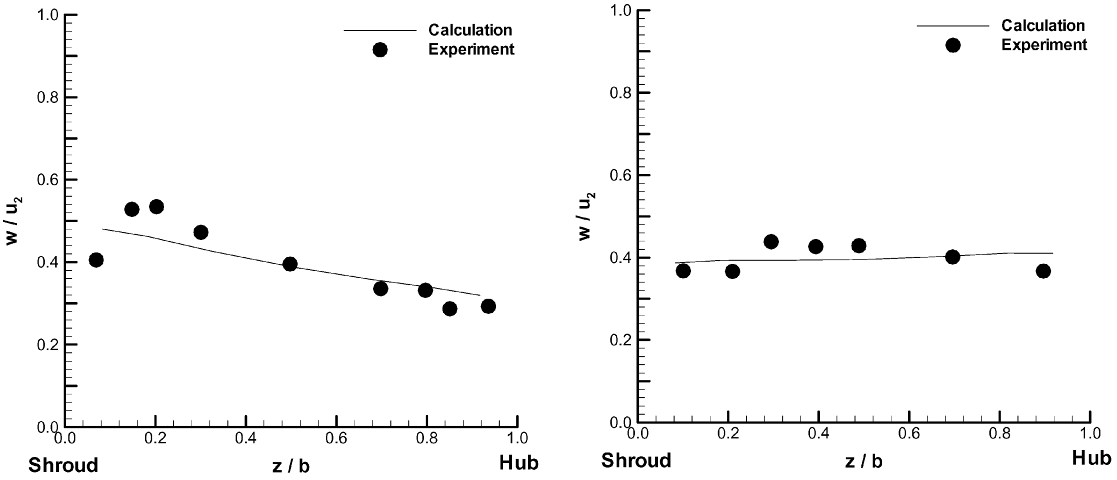

(c) Plane III (d) Plane IV

Fig. 2. Comparison of hub-to-shroud relative velocity distributions. (a) Plane I, (b) Plane II, (c) Plane III and (d) Plane IV.

$$C(\vec{r})p(\vec{r}) = \int_{S_Y} \left(G(\vec{r}, \vec{r}_Y) \frac{\partial p(\vec{r}_Y)}{\partial \hat{n}_Y} - \frac{\partial G(\vec{r}, \vec{r}_Y)}{\partial \hat{n}_Y} p(\vec{r}_Y) \right) \mathrm{d}S_Y, \tag{8}$$

where S_Y is the surface of the boundary element model, Y indicates a source point on the boundary element surface, $\vec{r}$ is the position vector for the data recovery point, $\vec{r}_Y$ is the position vector of a source point on the surface of the model, $\hat{n}_Y$ is the unit normal at the location of the source point, $C(\vec{r})$ is the integration constant resulting from the integration of Dirac's function originating from the fundamental solution to the governing differential wave equation, and $G(\vec{r}, \vec{r}_Y)$ denotes Green's function as follows.

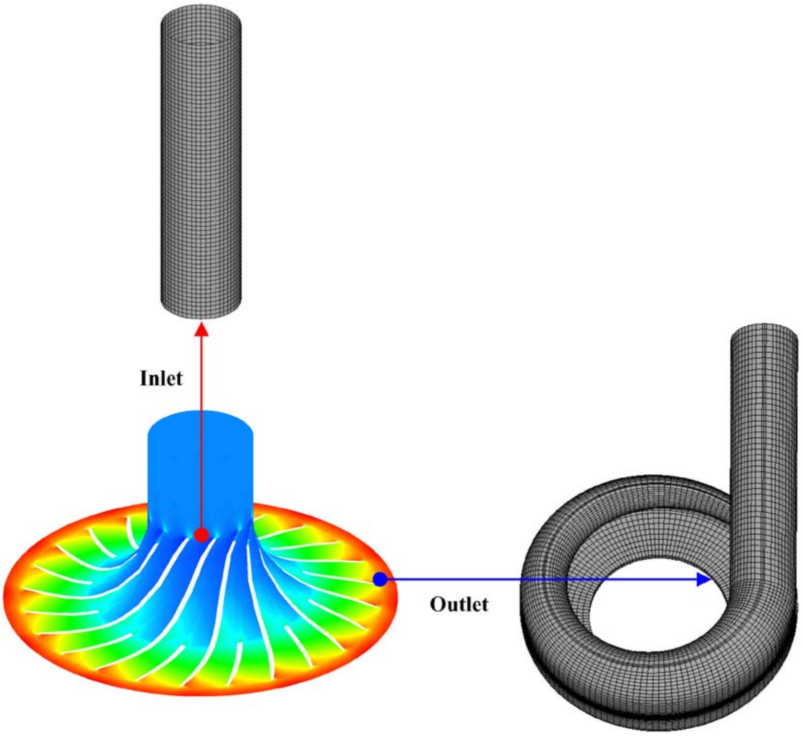

Fig. 3. Acoustic pressure boundary condition for boundary element analysis.

$$G(\vec{r},\vec{r}_Y)=\frac{1}{4\pi|\vec{r}-\vec{r}_Y|}\,\mathrm{e}^{-\mathrm{j}|\vec{r}-\vec{r}_Y|}. \tag{9}$$

In order to derive the integral equation for the indirect formulation, the standard approach used in indirect boundary element formulations is applied [13]. The integral equations for two acoustic spaces, Y_1 and Y_2 are added together. Within the integral, the terms which include Green's function are factored out and the opposite direction of the unit normal between two equations is taken into account in generating new primary variables. The equations for primary variables and the acoustic pressure at a data recovery point are

$$\delta p(\vec{r}_Y)=p(\vec{r}_{Y_1})-p(\vec{r}_{Y_2}),\quad \delta\,\mathrm{d}p(\vec{r}_Y)=\frac{\partial p(\vec{r}_{Y_1})}{\partial\hat{n}_{Y_1}}-\frac{\partial p(\vec{r}_{Y_2})}{\partial\hat{n}_{Y_2}},$$

$$p(\vec{r})=\int_{S_Y}\left(G(\vec{r},\vec{r}_Y)\delta\,\mathrm{d}p(\vec{r}_Y)-\frac{\partial G(\vec{r},\vec{r}_Y)}{\partial\hat{n}_Y}\,\delta p(\vec{r}_Y)\right)\mathrm{d}S_Y, \tag{10}$$

where $\delta p(\vec{r}_Y)$ is the difference in the pressure between the two sides of the boundary and $\delta\,\mathrm{d}p(\vec{r}_Y)$ is the difference in the normal gradient of the pressure [14].

A centrifugal compressor impeller model is selected to demonstrate the noise prediction capability. It consists of 12 impeller blades and 12 splitters and is designed at a speed of

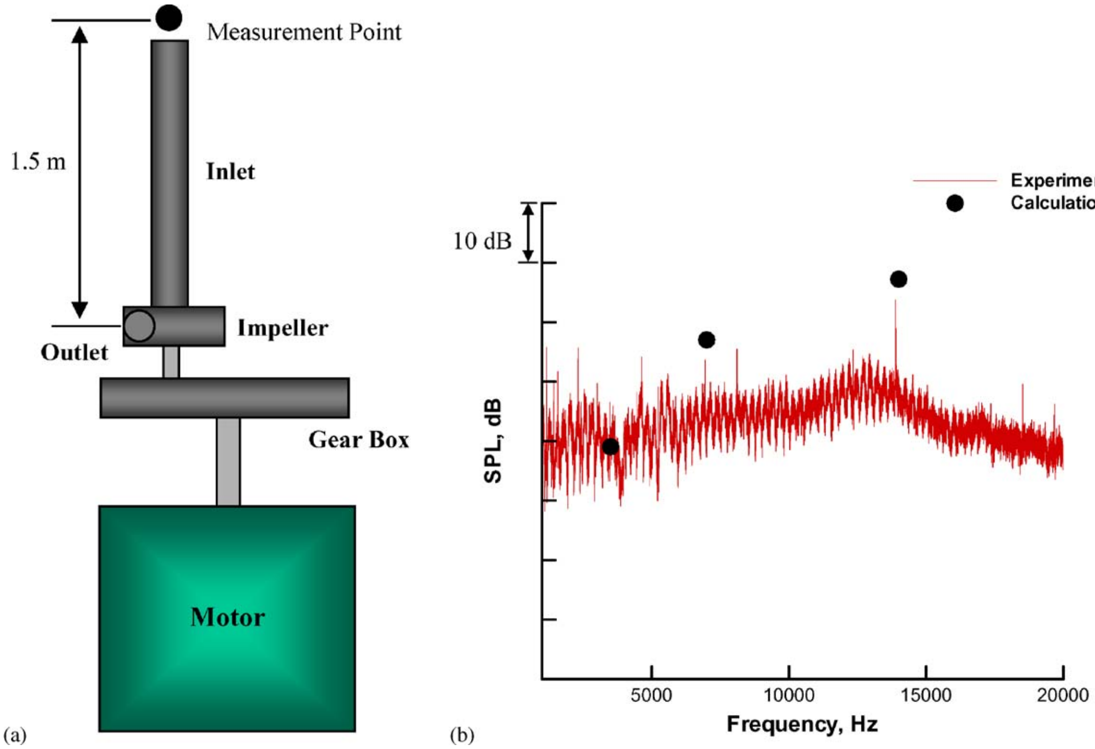

Fig. 4. (a) Experimental setup for noise measurement and (b) comparison of computational results and measured data.

70,000 rev/min. The fundamental blade passing frequency (hereafter, BPF) values in the inlet and outlet of the impeller are 14,000 and 28,000 Hz, respectively. The noise spectrum is measured at a distance of 1.5 m from the centrifugal compressor center (Fig. 4(a)). The position in front of the inlet duct end is chosen to minimize the influence of other noise components on the centrifugal compressor system. Sound pressure level (hereafter, SPL) values are computed at the fundamental BPF and sub-harmonic frequencies for the validation of the numerical method (Fig. 4(b)) and the numerical results at the discrete frequencies are predicted well.

4. Optimization design

The response surface model is usually assumed as a second-order polynomial, which can be written for n_v design variables below [1].

$$y^{(p)} = c_0 + \sum_i c_i x_i + \sum_{1 \leqslant i \leqslant j \leqslant n_v} c_{ij} x_i x_j, \quad p = 1, \ldots, n_s, \tag{11}$$

where $y^{(p)}$ is the dependent variable of the response surface model, c_0, c_i, c_{ij} are the regression coefficients, x_i is the design variable, and n_s is the number of observations.

The basis functions for the regression model of Eq. (11) lead to an overdetermined matrix problem and the regression coefficients are obtained to minimize the total statistical error.

$$\vec{y} = X\vec{c},$$

$$\vec{c} = (X^{\mathrm{T}}X)^{-1}X^{\mathrm{T}}\vec{y}, \tag{12}$$

where $\vec{y}$ is the response vector, X is the $n_s \times n_{\mathrm{rc}}$ matrix, n_{rc} is the number of regression coefficients, and $\vec{c}$ is the vector of the regression coefficients.

The candidate points are based on the three-level factorial design including D-optimal condition as a selection technique of data points in this study. The allowable range of each design variable is defined by lower and upper bounds prior to creating experimental design points. The three-level factorial design is created by specifying lower bound, midpoint, and upper bound $[-1, 0, 1]$ for each design variable. According to D-optimal criterion, the selected points are those that maximize the determinant, $|X^{\mathrm{T}}X|$. The data-points set that maximizes $|X^{\mathrm{T}}X|$ is the set of data points that minimizes the maximum variance of any predicted value from the regression model as well as the set of data points that minimizes the variance of regression coefficients.

Analysis of variance and regression analysis are the statistical techniques to estimate regression coefficients in the quadratic polynomial model and also yield a measure of uncertainty in the coefficients. The regression model expresses the relationship between responses and independent variables, which partially explains observations through fitted values. The relationship between the response and the approximation model can be represented as follows.

$$y_i = \hat{f}(x_i) + \varepsilon_i,$$

$$E(\varepsilon_i) = 0 \quad \text{and} \quad \mathrm{var}(\varepsilon_i) = \delta^2, \tag{13}$$

where $\hat{f}(x_i)$ is the response surface model and the random variables, ε_i are the errors that create the scatter around the linear relationship. It is assumed that these errors are mutually independent and normally distributed with mean zero and variance, δ^2. The variation of the responses, y_i and the fitted values, $\hat{y}_i$ about the mean, $\bar{y}$ can be measured in terms of total sum of squares (SSTO), regression sum of squares (SSR), and error sum of squares (SSE).

$$\mathrm{SSTO} = \sum_{i=1}^{n_s} (y_i - \bar{y})^2, \quad \mathrm{SSR} = \sum_{i=1}^{n_s} (\hat{y}_i - \bar{y})^2, \quad \mathrm{SSE} = \sum_{i=1}^{n_s} \varepsilon_i, \quad \mathrm{SSTO} = \mathrm{SSR} + \mathrm{SSE}. \tag{14}$$

One of the important statistical parameters is the coefficient of determination, R^2 which provides a summary statistic that measures how well the regression equation fits the data.

$$R^2 = \frac{\mathrm{SSR}}{\mathrm{SSTO}} = 1 - \frac{\mathrm{SSE}}{\mathrm{SSTO}}, \quad 0 \leqslant R^2 \leqslant 1. \tag{15}$$

In $R^2 = 0$, the regression model explains none of the variation in response values. On the other hand, $R^2 = 1$ means that all n_s observations lie on the fitted regression line and all of the variations are explained by the linear relationship with explanatory variables.

However, a large value of R^2 does not necessarily imply that the regression model is a good one. Adding a variable to the model will always increase R^2, regardless of whether the additional variable is statistically significant or not. Therefore, it is possible for the models that have a large value of R^2 to yield the poor predictions of the new observations of the estimates of the mean response. Because R^2 always increases as new terms are added to the model, using the *adjusted*-R^2 statistic is preferred.

$$R^2_{\mathrm{adj}} = 1 - \frac{\mathrm{SSE}/(n_s - n_{\mathrm{rc}})}{\mathrm{SSTO}/(n_s - 1)} = 1 - \left(\frac{n_s - 1}{n_s - n_{\mathrm{rc}}}\right)(1 - R^2). \tag{16}$$

In general, the *adjusted*-R^2 statistic will not always increase as new variables are added to the model. In fact, if unnecessary terms are added, the value of R^2_{adj} will often decrease.

5. Results and discussion

Eckardt 0-type impeller at the optimum design point (the same operating condition as that of the performance verification case) is used to carry out the low-noise impeller design study. The time-dependent pressure data of Eckardt 0-type impeller inlet and outlet are obtained from flow analysis, and are Fourier-transformed to examine the effect of unsteady flow variations which are the important BPF noise source of the rotating impeller. The pressure history in Fig. 5 shows the periodicity and the complicated shape in the impeller outlet is caused by the mixing flow of the impeller exit. The first BPF component of about 5000 Hz is dominant in the frequency domain and the design objective is focused on the reduction of the fundamental BPF noise source.

The low-noise impeller shape design includes the effect of six geometrical parameters, which are composed of impeller meridional configuration ($x_1 - x_4$ in Fig. 6), impeller blade camber line (x_5), impeller blade thickness (x_6). The range of selected design variables is adequately assigned for preventing the serious change of the impeller internal flow such as the separation phenomenon. The variations of design variables related to the impeller meridional configuration are presented in Fig. 6 and the particularly elegant technique developed by Bezier is used to consider the change of the impeller geometry. In Fig. 6, R is the impeller radial position and Z is the impeller vertical location. Bezier curves are defined by algebraic functions which allow the systematic and controlled variation of the shape, and which provide continuous derivatives up to any required degree. The curve is specified by the coordinates of a series of points in space of which only the first and last lie on the curve they define. The general form of Bezier polynomial of degree, n is given by [15]

$$\bar{R} = \sum_{k=0}^{n} \bar{P}_k B_k^n(u), \quad B_k^n(u) = \binom{n}{k} u^k (1-u)^{n-k}, \tag{17}$$

where $\bar{R}$ is the Bezier parametric curve function and $B_k^n(u)$ is the continuous function defining the curve with n discrete control points, $\bar{P}_k$ ($u = 0$ at the first control point and $u = 1$ at the last control point). The blade camber lines of Eckardt 0-type impeller have ellipsoidal shapes in cylindrical sections.

$$(Y - a)^2/a^2 + X^2/b^2 = 1, \tag{18}$$

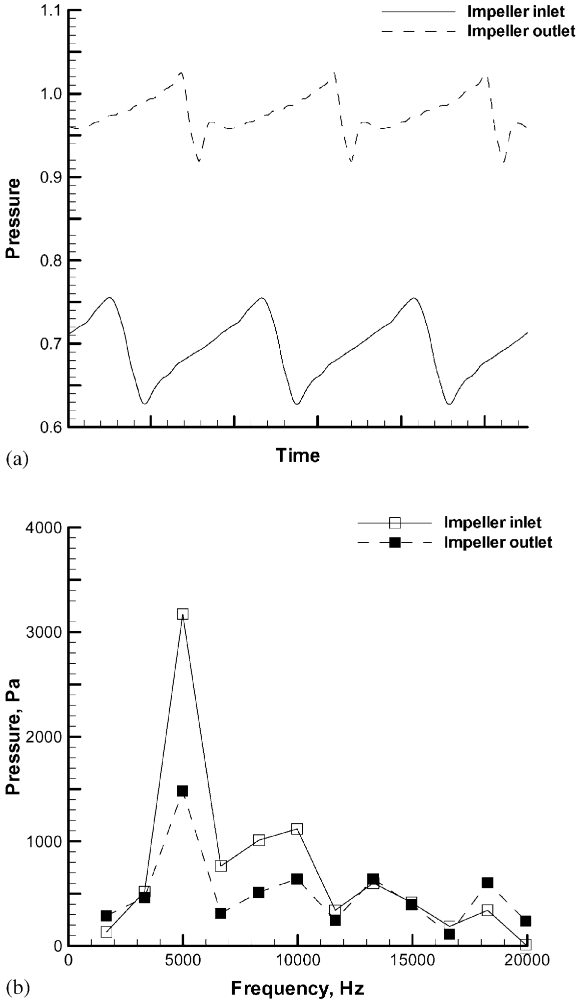

Fig. 5. Pressure fluctuations of impeller inlet and outlet. (a) Time domain, (b) frequency domain.

where X, Y are the coordinates of the ellipse, a, b are the circumferential half-axes of the ellipse, and the value of a varies with the impeller radial position, r.

$$a = 4.7693r\ (\text{mm}) \quad \text{and} \quad b = 220.579\ (\text{mm}). \tag{19}$$

The parameter, b of Eq. (19) is selected to look into the influence of the blade camber line change (design variable, x_5).

The inflow and outflow boundary conditions by mean line analysis are applied to include the effect of the impeller geometry change in the flow computation [16]. The mean line flow modeling is the simplest and the most informative method of considering the average characteristics of the flow which gives the correct representation for the entire flow field. The reasons why Eckardt 0-type impeller is chosen as the baseline impeller of the low-noise

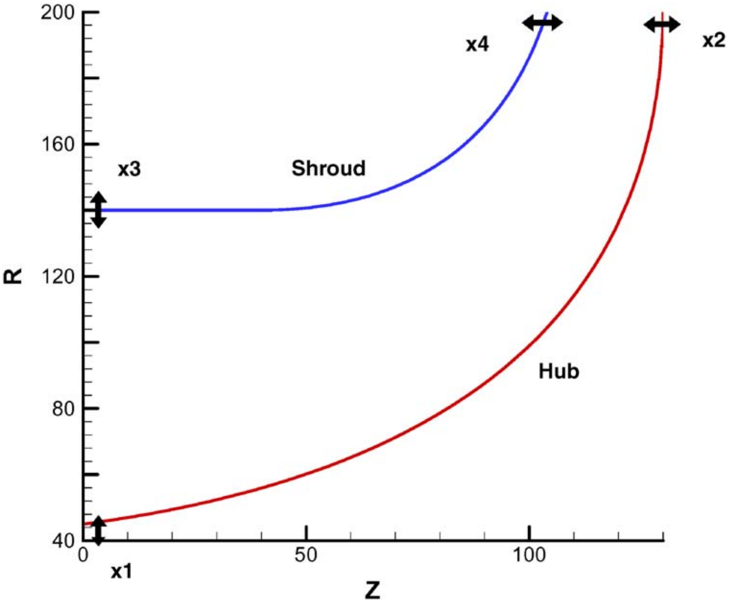

Fig. 6. Impeller meridional configuration variations.

optimization design are as follows: (1) The full geometric data of the impeller and the diffuser are available. (2) A radial impeller is simpler to calculate by hand than a backswept impeller. (3) A large body of experimental data exists. The flow information at impeller inlet, impeller tip, and diffuser exit is computed with the assumptions about slip factor, impeller efficiency, and diffuser pressure recovery.

The inflow boundary conditions at the impeller inlet are calculated by gas property relations and the meridional velocity, C_{m1t} which is given in terms of the impeller inlet area, A_{geo}. An iteration process is required to compute the static pressure, p_{1t} and temperature, T_{1t} using the total pressure, p_{01} and temperature, T_{01} in Fig. 7, where M_{1t} is the Mach number of the impeller inlet and R is the gas constant.

At the impeller tip, the meridional velocity, C_{m2m} is expressed using the mass flow rate, $\dot{m}$ and the tangential velocity, $C_{\theta 2m}$ is given by slip velocity, σU_2, meridional velocity, and impeller tip blade angle, β_{2b}.

$$U_2 = \frac{2\pi r_2 N}{60}, \quad C_{\theta 2m} = \sigma U_2 + C_{m2m} \tan \beta_{2b}, \tag{20}$$

where U_2 is the rotational velocity of the impeller tip, r_2 is the impeller radius, and N is the impeller angular velocity.

Because Eckardt 0-type impeller is designed with radial blades at exit, $\beta_{2b} = 0^{\circ}$. The slip velocity is defined as the difference between the idealized and actual tangential velocities. The slip factor, σ is the ratio of the actual tangential velocity to the idealized tangential velocity and Wiesner's slip factor correlation is applied [17,18].

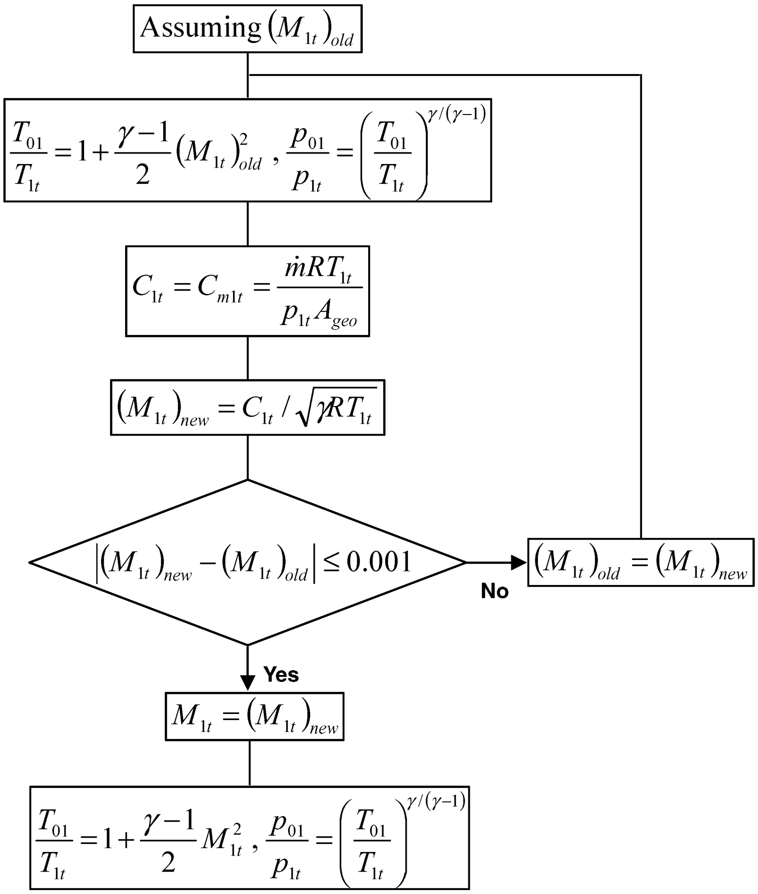

Fig. 7. Iteration process for computing impeller inflow boundary conditions.

$$\sigma = 1 - \frac{\sqrt{\cos\beta_{2b}}}{Z^{0.7}}, \tag{21}$$

where Z is the number of impeller blades.

The Euler turbomachinery equation is used to connect the work input to the impeller, W with the change in the total enthalpy, Δh_0 in relation to the swirl generated at exit [16], and the value of the impeller isentropic efficiency, η_{impeller} is assumed as 0.92 to take impeller losses into account.

$$W = \Delta h_0 = h_{02} - h_{01} = U_2 C_{\theta 2m}, \quad T_{02m} = T_{01} + \frac{\Delta h_0}{C_p}, \quad \frac{p_{02m}}{p_{01}} = \left(1 + \frac{\eta_{\text{impeller}}\Delta h_0}{C_p T_{01}}\right)^{\gamma/(\gamma-1)}, \tag{22}$$

where h_{01} is the total enthalpy of the impeller inlet, h_{02} is the total enthalpy of the impeller tip, p_{02m} is the total pressure of the impeller tip, T_{02m} is the total temperature of the impeller tip, and C_p is the specific heat at constant pressure.

The same iteration process as the calculation of the impeller inflow boundary condition is performed at the impeller tip in Fig. 8, where T_{2m} is the static temperature of the impeller tip, p_{2m}

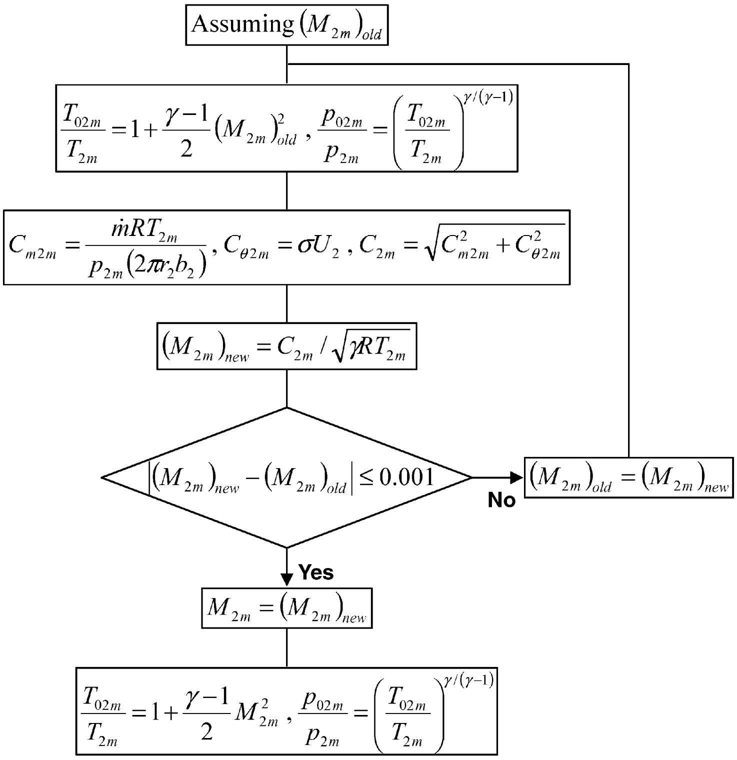

Fig. 8. Iteration process for computing impeller tip flow.

is the static pressure of the impeller tip, M_{2m} is the Mach number of the impeller tip, C_{2m} is the resultant velocity of the impeller tip, and b_2 is the width of the impeller tip.

The performance of the vaneless diffuser connected with Eckardt 0-type impeller is selected as outflow boundary conditions and can be specified in terms of the static pressure recovery coefficient, $C_{p,2m-5}$ [16].

$$p_5 = p_{2m} + C_{p,2m-5}(p_{02m} - p_{2m}), \quad C_{p,2m-5} = 0.35 \quad \text{at } r/r_2 = 1.3, \tag{23}$$

where p_5 is the static pressure of the diffuser exit and r is the radius of the diffuser exit.

Based on the computed pressure data of flow analysis, the SPL calculations of the first BPF from the impeller inlet and outlet are performed at a distance of 1 m from the impeller center (Fig. 9). Fifty-seven numerical simulations and 28 regression coefficients are used to construct the quadratic response surface model. Because the response surface model is the approximation model based on numerical results or experimental data, Table 1 shows the accuracy of the response surface model in the low-noise impeller design. In Table 1, r is the radial position. The percentage of root-mean-square error (hereafter, %RMSE) of Table 1 is defined as

$$\%\text{RMSE} = 100 \times \frac{\sqrt{1/n_s \sum_{i=1}^{n_s} (y_i - y_i^{(p)})^2}}{1/n_s \sum_{i=1}^{n_s} y_i} \tag{24}$$

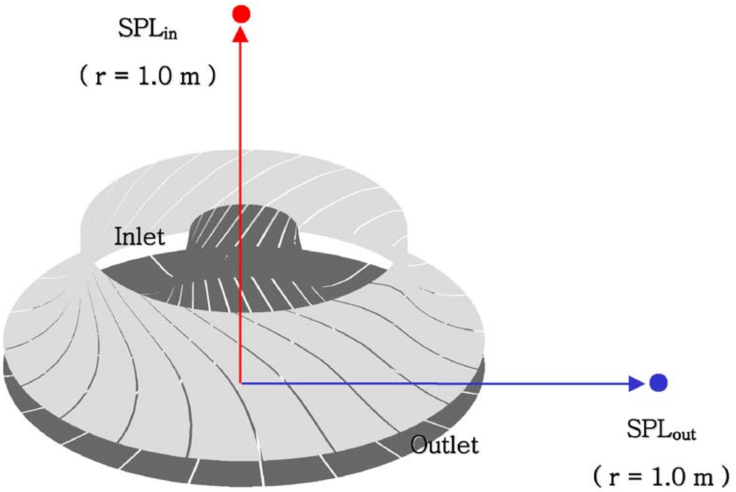

Fig. 9. Noise computation of impeller inlet and outlet.

Table 1
Fitting quality in low-noise impeller design

	R^2	R^2_{adj}	%RMSE
pr_{tt} [a]	1.000	1.000	0.0064
η_{tt} [b]	1.000	0.999	0.0668
SPL_{in} [c]	0.905	0.817	2.7102
SPL_{out} [d]	0.997	0.994	0.0277

[a] Total-to-total pressure ratio at $r/r_2 = 1.075$.
[b] Total-to-total efficiency at $r/r_2 = 1.075$.
[c] SPL value from impeller inlet, dB.
[d] SPL value from impeller outlet, dB.

R^2, the coefficient of multiple determinations, is a measure of the amount of reduction in variability of y_i obtained by using design variables and has the value between 0 and 1. Table 1 proves that the aerodynamic performance and noise characteristics depending on the impeller shape change can be well predicted with the quadratic model, although the accuracy of the SPL distribution from the impeller inlet is a little lower than that of other quantities due to the influence of boundary conditions according to the impeller geometry change. Therefore, the quadratic model is sufficient to consider non-smooth and noisy objective functions and constraints for turbulent flows in the low-noise impeller design.

It is important to examine the influence of design parameters on the impeller aerodynamic performance and noise from the viewpoint of deciding the optimization design scope. This can be seen clearly by the t-statistic value distribution in Fig. 10, which shows the result of linear terms in

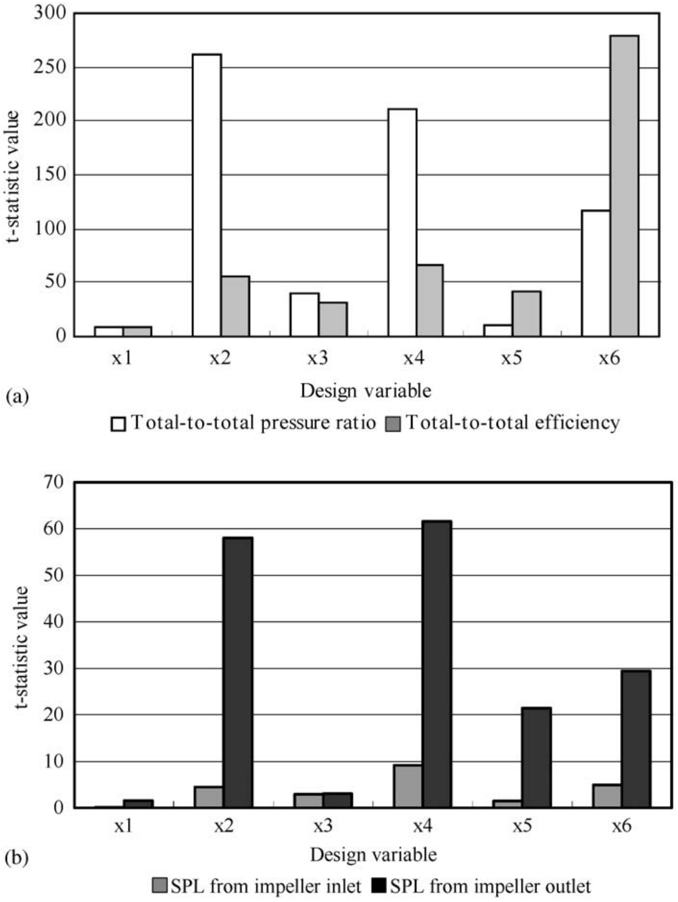

Fig. 10. Comparison of *t*-statistic value in low-noise impeller design. (a) Impeller performance, (b) impeller noise.

the response surface model. Here, *t*-statistic is defined as

$$t = \frac{c_j}{\sqrt{\hat{\sigma}^2 C_{jj}}}, \quad j = 1, \ldots, n_{\mathrm{rc}}, \tag{25}$$

where $\hat{\sigma}^2$ is the estimation of variance and C_{jj} is the diagonal element of $(X^{\mathrm{T}}X)^{-1}$ corresponding to c_j. The design variable of a higher *t*-statistic value has a more dominant effect on the response surface model. This implies that design results can be improved by increasing the variation range of dominant terms or by adding more design variables in the dominant region within the bounds of satisfying the fitting quality in the response surface model. In the impeller meridional configuration, the design variables, x_2 and x_4 corresponding to the modification of the impeller blade tip shape have higher *t*-statistic values than the design parameters, x_1 and x_3 related to the impeller inlet part due to the boundary condition variation according to the change of the impeller blade geometry. The effects of the blade camber line and the blade thickness are also observed, because they have an influence on the impeller internal flow passage.

Table 2
Objective function and constraint for optimization process

	Objective function	Constraint
Case 1	η_{tt} maximum	$\mathrm{pr}_{tt} \geqslant (\mathrm{pr}_{tt})_{\mathrm{baseline}}$
Case 2	$\mathrm{SPL}_{\mathrm{in}}$ minimum	$\mathrm{pr}_{tt} \geqslant (\mathrm{pr}_{tt})_{\mathrm{baseline}}$
Case 3	$\mathrm{SPL}_{\mathrm{out}}$ minimum	$\mathrm{pr}_{tt} \geqslant (\mathrm{pr}_{tt})_{\mathrm{baseline}}$

Table 3
Comparison of impeller performance results

	pr_{tt}		η_{tt}	
	Response surface model	Numerical simulation	Response surface model	Numerical simulation
Baseline	2.0940		0.9137	
Case 1	2.1020	2.1025	0.9366	0.9377
Case 2	2.0943	2.0971	0.9267	0.9286
Case 3	2.0969	2.0943	0.9289	0.9271
Case 4	2.0940	2.0944	0.9275	0.9263

One of the greatest advantages of RSM is that the performance computation and noise prediction do not need to be repeated as objective functions and constraints are changed. It is a key point to decide the method to formulate objective functions and constraints after all calculations are performed. Therefore, four kinds of design problems (Table 2 and Eq. (27)) are applied to investigate the influence of objective functions and constraints on the impeller performance and noise, which include the multi-objective capability by the weighting objective method. The weighting objective method takes each objective function and multiplies it by a fraction of one, the weighting factor, we_j. The modified functions are then added together to obtain a single cost function. Mathematically, the new function is written as

$$f(X) = \sum_{j=1}^{k} we_j f_j(X), \quad 0 \leqslant we_j \leqslant 1, \quad \sum_{j=1}^{k} we_j = 1, \tag{26}$$

where $f_j(X)$ is the objective function and k is the number of objective functions. The objective function with the weighting factors of $we_1 = we_2 = we_3 = 0.3333$ and the constraint in Case 4 are selected below.

$$\begin{aligned} &\text{Objective: minimize } we_1/\eta_{tt} + we_2 \times \mathrm{SPL}_{\mathrm{in}} + we_3 \times \mathrm{SPL}_{\mathrm{out}} \\ &\text{Subject to: } \mathrm{pr}_{tt} \geqslant (\mathrm{pr}_{tt})_{\mathrm{baseline}}, \end{aligned} \tag{27}$$

where *baseline* means the baseline impeller.

With the constructed response surface model, genetic algorithm (hereafter, GA) optimization is performed to obtain the optimum solution of a defined objective function with the penalty terms

Table 4
Comparison of impeller noise results

	SPL_{in}		SPL_{out}	
	Response surface model	Numerical simulation	Response surface model	Numerical simulation
Baseline	81.1406		109.5489	
Case 1	74.9566	72.7031	110.0878	110.4567
Case 2	68.3209	71.3055	109.5064	109.7714
Case 3	68.1932	89.5307	109.7679	109.1150
Case 4	93.6468	76.5927	109.0661	109.5000

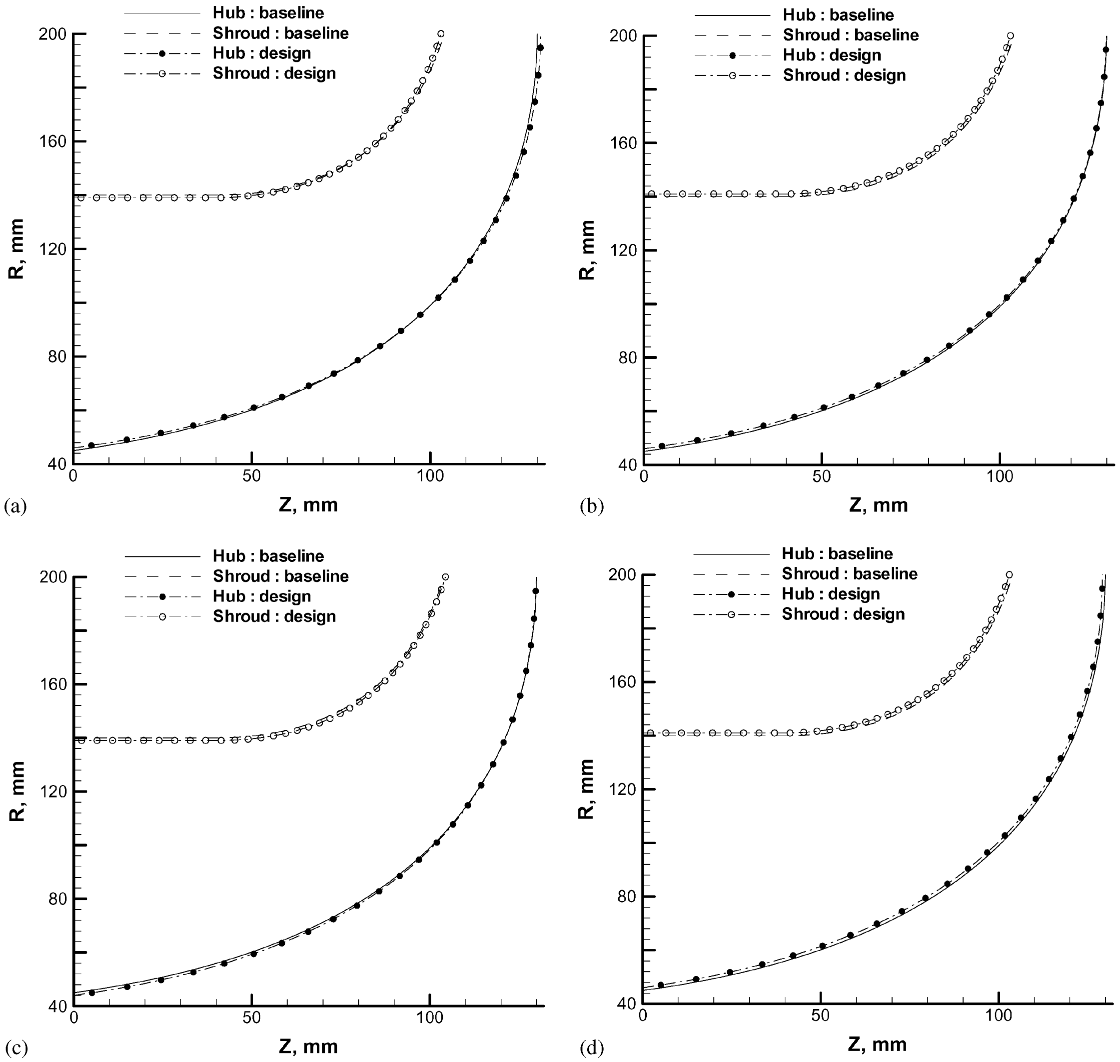

Fig. 11. Comparison of impeller geometry. (a) Case 1, (b) Case 2, (c) Case 3 and (d) Case 4.

of constraints. Tables 3 and 4 show the comparison of the impeller performance and noise level in baseline and optimized impeller blades using the response surface model and the resulting numerical simulation. The difference between response surface model results and numerical simulation results is small with the exception of the impeller inlet noise due to the response surface model accuracy of the impeller inlet noise. This result proves the importance of the fitting quality of the response surface model to enhance the usefulness of the optimization design. The comparison analysis of the impeller performance displays the improvement of the total-to-total efficiency, η_{tt} satisfying the constraint condition of the total-to-total pressure ratio, pr_{tt}. The positive effect with the exception of Case 3 is seen in the design result of the impeller inlet noise, $\mathrm{SPL}_{\mathrm{in}}$. The small decrease in the impeller outlet noise, $\mathrm{SPL}_{\mathrm{out}}$ is caused by the noise level objective function as well as the small perturbation of design variables. The result of the multi-objective optimization design (Case 4) shows the impeller performance increase and the impeller noise reduction. Fig. 11 exhibits the impeller meridional configurations of optimized impeller blades in the low-noise impeller design, which shows the various change according to the characteristics of design problems. The design results of the impeller blade camber line (optimized value of b in Eq. (19)) are higher than the value of the baseline impeller within the framework of the impeller flow stabilization due to the decrease of the impeller blade angle. The decrease of the optimized blade thickness has an influence on the reduction of the flow variation by the rotating impeller blade.

6. Concluding remarks

The present work is focused on introducing an efficient and robust optimization method to develop the advanced impeller geometry with the high performance and the low noise. The design procedure including RSM and GA is combined with Navier–Stokes solver for impeller flow analysis and FW–H equation for the impeller noise prediction. The statistical approach is used to guarantee the accuracy of the optimization design, and the t-statistic values are calculated to give a more information about the influence of design variables on the impeller performance and noise. The advanced impeller geometry and the improvement of the impeller performance and noise are obtained from the optimization design process. Although RSM has a limitation on the number of design variables due to the computational cost and the range of design variables is a little narrow because of the response surface model accuracy, this technology can be a viable optimization tool for the impeller aerodynamic/aeroacoustic design.

Acknowledgements

This work is supported by Samsung Techwin Co., Ltd. in Korea, International Cooperative Research Program of Korea Institute of Science and Technology Evaluation and Planning (KISTEP), and National Research Laboratory (NRL) Program of Ministry of Science and Technology in Korea.

References

[1] R.H. Myers, D.C. Montgomery, *Response Surface Methodology: Process and Product Optimization Using Designed Experiments*, Wiley, New York, 1995.

[2] J. Ahn, H. Kim, D. Lee, O. Rho, Response surface method for airfoil design in transonic flow, *Journal of Aircraft* 38 (2001).

[3] D.C. Wilcox, *Turbulence Modeling for CFD*, DCW Industries Inc., 1993.

[4] P.L. Roe, Approximate Riemann solvers, parameter vectors, and difference schemes, *Journal of Computational Physics* 43 (1981) 357–372.

[5] P.K. Sweby, High resolution TVD schemes using flux limiters, *Lectures in Applied Mathematics* 22 (1985) 289–309.

[6] T.H. Pulliam, D.S. Chaussee, A diagonal form of an implicit approximate-factorization algorithm, *Journal of Computational Physics* 39 (1981) 347–365.

[7] J.L. Thomas, R.W. Walters, T. Reu, F. Ghaffari, R.P. Weston, J.M. Luckring, Application of a patched-grid algorithm to the F/A-18 forebody-leading-edge extension configuration, *Journal of Aircraft* 27 (1990) 749–756.

[8] D. Eckardt, Flow field analysis of radial and backswept centrifugal compressor impellers—Part 1: flow measurements using a laser velocimeter, in: *The 25th Annual International Gas Turbine Conference*, New Oreans, Louisiana, March 9–13, 1980, pp. 77–86.

[9] P. Schuster, U. Schmidt-eisenlohr, Flow field analysis of radial and backswept centrifugal compressor impellers—Part 2: comparison of potential flow calculations and measurements, in: *The 25th Annual International Gas Turbine Conference*, New Oreans, Louisiana, March 9–13, 1980, pp. 87–95.

[10] A.P. Dowling, J.E. Ffowcs Williams, *Sound and Sources of Sound*, Wiley, New York, 1983.

[11] W. Jeon, D. Lee, A numerical study on the flow and sound fields of centrifugal impeller located near a wedge, *Journal of Sound and Vibration* 266 (2003) 785–804.

[12] R.D. Cickowski, C.A. Brebbia, *Boundary Element Methods in Acoustics*, Elsevier Applied Science, New York, 1991.

[13] P.K. Banerjee, *The Boundary Element Methods in Engineering*, McGraw-Hill, New York, 1994.

[14] T.W. Wu, *Boundary Element Acoustics*, WIT Press, Southampton, 2000.

[15] M.V. Casey, A computational geometry for the blades and internal flow channels of centrifugal compressors, *Journal of Engineering for Power* 105 (1983) 288–295.

[16] D. Japikse, N.C. Baines, *Introduction to Turbomachinery*, Concepts ETI Inc., and Oxford University Press, USA, Oxford, 1994.

[17] N.A. Cumpsty, *Compressor Aerodynamics*, Longman Scientific & Technical, England, 1989.

[18] D. Japikse, *Centrifugal Compressor Design and Performance*, Concepts ETI Inc., USA, 1996.